

SEARCH FOR THE STANDARD MODEL HIGGS BOSON IN THE \cancel{E}_T AND
B-JET SIGNATURE IN PROTON-ANTIPROTON COLLISIONS AT A CENTER
OF MASS ENERGY OF 1.96 TEV

A Preliminary Report
Submitted to the Faculty
of
Purdue University
by
Artur Apresyan

September 2007
Purdue University
West Lafayette, Indiana

TABLE OF CONTENTS

	Page
LIST OF TABLES	iv
LIST OF FIGURES	v
ABSTRACT	vi
1 Introduction	1
2 The Higgs Boson	3
2.1 Introduction	3
2.2 Spontaneous Symmetry Breaking	4
2.3 Searches of Higgs Boson	7
3 Experimental Apparatus	9
3.1 The Tevatron	9
3.2 The CDF II detector	9
3.3 The Tracking System	11
3.3.1 Silicon Vertex Detector	12
3.3.2 Central Outer Tracker	12
3.4 Calorimeter	12
3.5 Muon Detector	13
3.6 Time of Flight Detector	13
3.7 Luminosity Counting	14
3.8 Trigger and Data Acquisition	15
4 Analysis	16
4.1 Event Selection and Triggger Path	16
4.1.1 Event Kinematics	16
4.1.2 Trigger Path and Data Sample	16
4.1.3 \cancel{E}_T Clean-up	17

	Page
4.1.4 Jet E_T and \cancel{E}_T Reconstruction	18
4.1.5 B-tagging	18
4.1.6 Pre-selection cuts	20
4.2 Signal and Background Simulation	21
4.2.1 Signal Monte Carlo	21
4.2.2 Background Simulation	21
4.3 Control and Signal Region Definitions	24
4.3.1 Definition of Control Regions	24
4.3.2 Control Region 1	26
4.3.3 Control Region 2	27
4.3.4 Signal Region	28
4.4 Systematic Uncertainties and Limit Calculation	30
4.4.1 Expected and Observed Limits	31
A Summary	38
LIST OF REFERENCES	39

LIST OF TABLES

Table		Page
4.1	The cross-section of the ZH/WH processes at various Higgs masses, the branching fractions $Br(Z \rightarrow \nu\bar{\nu}) = 0.2$ and $Br(W \rightarrow l\nu) = 0.32$ taken into account (i.e. number of Higgs produced in the 1 fb^{-1} data)	21
4.2	Monte Carlo background samples	22
4.3	Number of expected background events in the control regions in Single Tight Taged events (loose lepton selection).	25
4.4	Number of expected background events in the control regions in Double Loose Taged events (loose lepton selection).	26
4.5	Expected and observed background in Control Region 2 after tight lepton selection.	28
4.6	Acceptance on the signal in the signal region. The events were weighted by cross-section and efficiencies after applying the final selection. . . .	29
4.7	Number of expected background and signal events in the signal region after applying the final cuts.	31
4.8	The predicted and observed cross-section limits of the ZH and WH processes combined when $H \rightarrow b\bar{b}$ divided by the SM cross-section where Z decays to neutrinos and W decays leptonically	32

LIST OF FIGURES

Figure	Page
1.1 Standard Model Higgs production cross-ections at Tevatron (<i>left</i>) and branching ratios (<i>right</i>)	1
2.1 The Higgs potential.	5
2.2 Constraints on Higgs Mass from latest Tevatron measurement	8
3.1 Scehamatic view of the Teavtron	10
3.2 CDF II detector.	11
3.3 Cross section view of the CDF II tracking and calorimetry subsystems.	11
3.4 Map of the muon coverage as a function of azimuthal angle ϕ and pseudorapidity η	13
3.5 Schematic view of the luminosity monitor	14
3.6 Block diagram showing the CDF Run II trigger system	15
4.1 Schematic view of the secondary vertex tagging algorithm	19
4.2 Dijet invariant mass in the Signal Region, single- and double-tagged events	30
4.3 The Cross-Section upper limits	33
4 Control Region 1, Exclusive Single Tag plots from the top: 1 st jet E_T , 2 nd jet E_T , dijet mass	34
5 Control Region 1, Double Loose Tag plots from the top: 1 st jet E_T , 2 nd jet E_T , dijet mass	35
6 Control Region 2, Exclusive Single Tag plots after tight lepton selection from the top: 1 st jet E_T , 2 nd jet E_T , dijet mass	36
7 Control Region 2, Double Tag plots after tight lepton selection from the top: 1 st jet E_T , 2 nd jet E_T , dijet mass	37

ABSTRACT

Apresyan, Artur , Purdue University, September, 2007. Search for the Standard Model Higgs boson in the \cancel{E}_T and b-jet Signature in proton-antiproton collisions at a center of mass energy of 1.96 TeV. Major Professor: Daniela Bortoletto.

We search for the Higgs boson produced in association with a Z or a W boson. We consider a scenario where the Z decays into neutrinos or the lepton originating from the W-decay escapes detection and the Higgs decays into a $b\bar{b}$ pair. Therefore the expected signature is missing transverse energy, no leptons, and two b-jets. We process 1.7 fb^{-1} of data collected in $p\bar{p}$ collisions at $\sqrt{s} = 1.96 \text{ TeV}$ in Run II of the Tevatron. No significant excess above backgrounds is observed, so we set limits on associated Higgs boson production cross-section for Higgs masses in range from 110 to 150 GeV/ c^2 .

1. INTRODUCTION

In the Higgs mechanism of the Standard Model, the fermions and weak gauge bosons acquire mass via interaction with the Higgs field. The observable quantum of the fourth Higgs field is called the Higgs boson. The existence of this undiscovered particle is the cornerstone of the Standard Model [1].

At the Tevatron, the most probable production mode of the Higgs is by gluon fusion through a virtual top loop (Fig.1.1, left). Around 70% of the Higgs would decay into two b-quarks (Fig.1.1, right) yielding two b-jets in the final state. Since the QCD b-quark production is an irreducible background, this analysis would have a low sensitivity. The second most frequent production mode is when a virtual W or Z decays into a W or Z and a Higgs. In this case, it is possible to trigger on the decay products of the W/Z boson and significantly reduce the QCD background.

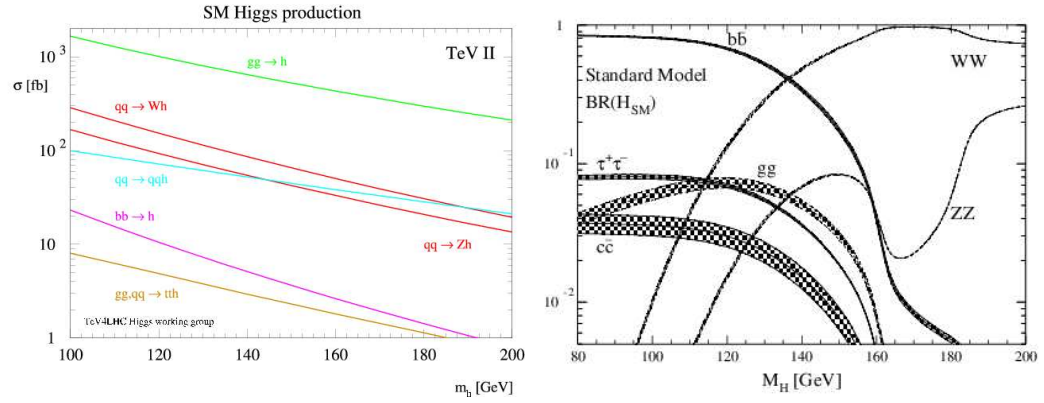


Fig. 1.1. Standard Model Higgs production cross-sections at Tevatron (*left*) and branching ratios (*right*)

We are analyzing Z-Higgs and W-Higgs associated productions when the Z decays into two neutrinos, or the W decays leptonically but the charged lepton escapes the

detection. Because the neutrinos will not be detected in the detector, either, they lead to an unbalanced transverse energy sum in the transverse plane (Missing Transverse Energy \cancel{E}_T). We are performing an unbiased analysis in which all the considerable Standard Model background processes, such as QCD heavy flavor multi-jet production, top production, and electro-weak processes, are simulated. After obtaining a good agreement between data and background prediction in control regions, we perform an optimization of the signal selection cuts on the Monte Carlo simulation. This way, the final selection in the signal region remains completely unbiased.

2. THE HIGGS BOSON

2.1 Introduction

The Standard Model, the theory which describes electromagnetic, weak and strong interactions is based on the local symmetry of the following form:

$$SU(2)_{I_W} \times U(1)_{Y_W} \times SU(3)_c,$$

where the local (gauge) groups act on the weak isospin I_W , the weak hypercharge Y_W and the color c relevant for the strong interactions. The electric charge Q is related to the above “weak charges” as follows:

$$Q = I_W + \frac{Y_W}{2}.$$

Imposing the gauge symmetry we have W/Z gauge bosons mediating the electro-weak interactions to be massless and the fermions’ masses will be zero as well (the corresponding mass terms in the Lagrangian density would violate the gauge symmetry).

The way to obtain a mass of gauge bosons W/Z , while preserving a local gauge symmetry, leads to the concept of the spontaneous symmetry breaking, which does not rely on the additional mass terms in the Lagrangian, but rather on the assumption that there exists a scalar field with a specific form of interaction, responsible for the mass of all the particles. Mass then appears not as a result of emission and absorption of quanta of the scalar field, but as a result of the interaction with the classical part of the scalar field, which extends over all space [2].

The spontaneous symmetry breaking, called the Higgs mechanism if applied to the local symmetry, is then considered as an ‘origin’ of the mass of fermions and

gauge bosons in the Standard Model. The existence of the Higgs scalar is expected to be the direct physical manifestation of this mechanism. Looking for a Higgs boson is therefore a challenge for the particle physics.

2.2 Spontaneous Symmetry Breaking

Let us consider how the Higgs mechanism works for a system containing a gauge boson A^μ . Here one introduces one complex scalar boson field Φ . The interaction with the gauge boson is described by the Lagrangian density with a local gauge group U(1) in the following form:

$$\mathcal{L} = (D_\mu \Phi)(D^\mu \Phi)^* + \mu^2 \Phi^* \Phi - \lambda(\Phi^* \Phi)^2 - \frac{1}{4} F^{\mu\nu} F_{\mu\nu}, \quad (2.1)$$

where

$$F^{\mu\nu} = \partial^\mu A^\nu - \partial^\nu A^\mu. \quad (2.2)$$

The covariant derivative

$$D^\mu = \partial^\mu + igA^\mu \quad (2.3)$$

contains the term related to the interaction between the scalar and the gauge field with a coupling g . The considered Lagrangian density is manifestly symmetric under the local U(1) symmetry transformation.

The parameters in the potential part:

$$V = -\mu^2 \Phi^* \Phi + \lambda(\Phi^* \Phi)^2, \quad (2.4)$$

are both positive,

$$\mu^2 > 0 \quad \text{and} \quad \lambda > 0, \quad (2.5)$$

leading to the potential bounded from below. (negative μ^2 would correspond to the mass term for Φ .) The potential (2.4) has minima for

$$| \langle \Phi \rangle | = \frac{1}{\sqrt{2}} v = \sqrt{\frac{\mu^2}{2\lambda}}, \quad (2.6)$$

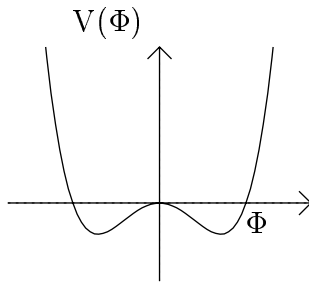


Fig. 2.1. The Higgs potential.

where v is called a vacuum expectation value. The example is shown in Fig. 2.1 for the one real field ϕ , where two minima appear. By choosing one of these minima as a true minimum of the energy, the symmetry of the physical system (the lowest (the vacuum) and higher excited states) is *spontaneously broken*.

The original $\Phi(x)$ field can be expressed by new real fields, ξ and h , with a zero vacuum expectation values, as in:

$$\Phi(x) = \frac{e^{i\xi/v}}{\sqrt{2}}(v + h(x)), \quad (2.7)$$

and further by choosing a particular gauge with $\xi=0$ we get

$$\begin{aligned} \mathcal{L} = & \frac{1}{2}(\partial_\mu - igA_\mu)(v + h)(\partial^\mu + igA^\mu)(v + h) \\ & + \frac{\mu^2}{2}(v + h)^2 - \frac{\lambda}{4}(v + h)^4 - \frac{1}{4}F^{\mu\nu}F_{\mu\nu} = \\ & \frac{1}{2}(\partial_\mu h)(\partial^\mu h) - \mu^2 hh + \frac{(gv)^2}{2}A^\mu A_\mu + g^2v hA_\mu A^\mu + .. \end{aligned} \quad (2.8)$$

Interpreting the individual terms in the Lagrangian density \mathcal{L} one can find that the considered theory contains:

- a mass term for the gauge boson $M = gv$,
- a neutral scalar boson h (a real field) with a mass $\sqrt{2}\mu$,
- the interaction terms $gM hA^\mu A_\mu$ with the coupling proportional to the mass of the gauge boson,

- the self interaction terms hhh , $hhhh$ etc.

By measuring the gauge boson mass one can determine the parameter v , provided there is independent constraint on the coupling g :

$$M = gv. \quad (2.9)$$

However to obtain the mass of the Higgs boson we should know in the addition the self interaction, i.e. parameter λ , since

$$M_h = \sqrt{2\lambda}v. \quad (2.10)$$

To generalize Higgs mechanism for $SU(2)_{I_W} \times U(1)_{Y_W} \times SU(3)_c$ group we introduce a complex scalar $SU(2)_{I_W}$ doublet

$$\Phi = \begin{pmatrix} \phi^+ \\ \phi^0 \end{pmatrix},$$

The electroweak sector in SM is described by a covariant derivative:

$$D^\mu = \partial^\mu + ig\frac{\vec{\tau}}{2}\vec{W}^\mu + ig'\frac{Y_W}{2}B^\mu, \quad (2.11)$$

where the ratio of couplings g and g' is described by the Weinberg angle θ_W , $\tan \theta_W = g'/g$. The original vector gauge fields:

$$W_1^\mu, W_2^\mu \text{ and } W_3^\mu, B^\mu \quad (2.12)$$

after mixing between the neutral fields, lead to the following physical charged and neutral fields

$$W_\mu^+, W_\mu^- \text{ and } Z_\mu, A_\mu, \quad (2.13)$$

with the corresponding particles known as W^\pm , Z bosons and the photon, γ . They mediate the so called charged (CC), neutral current (NC) processes and electromagnetic processes, respectively.

In addition to giving masses to the gauge bosons, the interaction of scalar field leads to masses of fermions. Namely for f_L being a SU(2) doublet and f_R a SU(2) singlet we get a mass term for the fermion f

$$g_f[(\bar{f}_L\Phi)f_R + hc] \rightarrow \frac{g_f v}{\sqrt{2}}(\bar{f}f). \quad (2.14)$$

Here g_f is the so called Yukawa coupling for fermion f . The parameter in front of the bracket in (2.14) for obvious reason should be interpreted as a mass of a fermion f , and therefore

$$m_f = \frac{g_f v}{\sqrt{2}}. \quad (2.15)$$

So, the scalar field generates mass terms for fermions. However the fermions' masses are not fixed by the parameters of the Higgs potential, nor the fermion mass pattern can be driven from the assumed mechanism.

2.3 Searches of Higgs Boson

One of the main physics goals of LEP2, the e^+e^- collider operated at CERN from 1995 to 2000, were the search for the Higgs. The Standard Model Higgs could in principle be produced at LEP2 in the reaction $e^+e^- \rightarrow ZH$ which proceeds by Z exchange. The non observation of the Higgs particle at LEP2 has allowed to establish a lower limit on its mass: $m_H \gtrsim 114 \text{ GeV}$.

Indirect indications on the Higgs mass were also obtained from the precision tests of the SM, as the radiative corrections effects depend logarithmically on m_H . According to the latest CDF and DØ combined result based on the new values for the W boson and top quark masses the upper limit on Higgs mass is $144 \text{ GeV}/c^2$ with 95 percent probability.

The experimental sensitivity for directly observing the Higgs boson at Tevatron is steadily improving. The Tevatron experiments are within reach of directly excluding a Higgs boson with mass near $160 \text{ GeV}/c^2$. Searches for a Higgs boson with lighter mass will require more data.

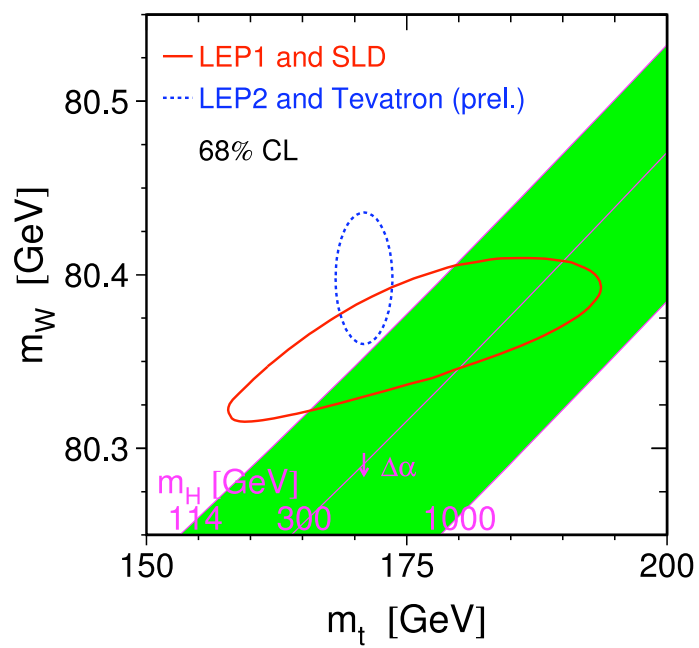


Fig. 2.2. Constraints on Higgs Mass from latest Tevatron measurement

3. EXPERIMENTAL APPARATUS

3.1 The Tevatron

The Tevatron is a proton-antiproton superconducting collider at the Fermi National Accelerator Laboratory (FNAL) in Batavia, Illinois. It currently operates with 36 proton on 36 antiproton bunches at a center-of-mass energy of $\sqrt{s} = 1.96 \text{ TeV}$ and a bunch spacing of 396 ns.

In collider operations the Tevatron takes 150 GeV protons and antiprotons provided by the main injector and accelerates them to 980 GeV. Fig.3.1 provides a schematic view of the Fermilab accelerator complex.

Proton and antiproton bunches circulate around the Tevatron in opposite directions. Their orbits cross at the B0 and D0 collision points, where interactions are observed by the CDF and DØ detectors respectively.

3.2 The CDF II detector

The Collider Detector at Fermilab (CDF II) [3] shown in 3.2 is a multipurpose experiment with azimuthal and forward-backward symmetry, designed to study high energy $p\bar{p}$ collisions. It combines precision charged particle tracking with fast projective calorimetry together with fine grained muon detection. The tracking system is contained inside a superconducting solenoid of 4.8 m length and 1.5 m radius. It generates a 1.4 T magnetic field parallel to the beam axis. The magnetic field is uniform with an accuracy of 0.1% throughout the entire tracking volume. The muon and calorimetry systems are located outside of the solenoid.



Fig. 3.1. Schematic view of the Tevatron

CDF uses a coordinate system with the positive z -axis lies along the direction of the incident proton beam, ϕ is the azimuthal angle, θ is the polar angle (measured from the detector center). The rapidity, y , of a particle is given by

$$y = \frac{1}{2} \ln \left(\frac{E + p_z}{E - p_z} \right).$$

Rapidity differences are useful in physics analysis, since they are invariant to a Lorentz boost. The pseudo-rapidity, η , is defined as $\eta = -\ln(\tan \frac{\theta}{2})$. The pseudo-rapidity η equals the rapidity y in the massless approximation ($E \gg mc^2$). Figure 3.3 shows the η -coverage of the individual components of the CDF tracking system.

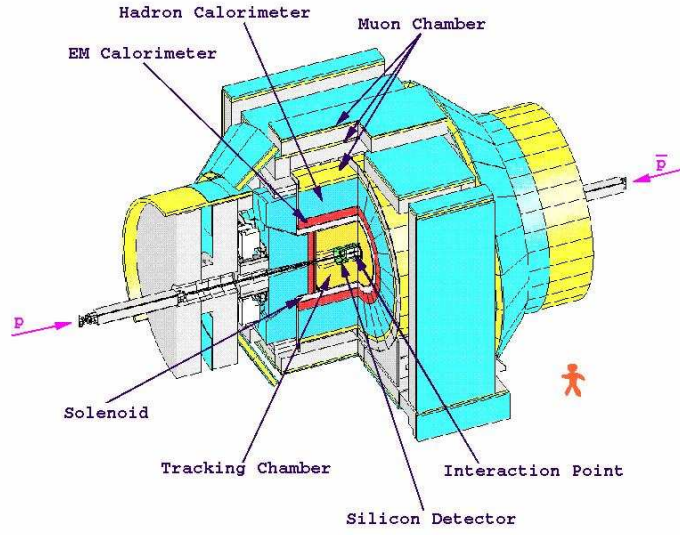


Fig. 3.2. CDF II detector.

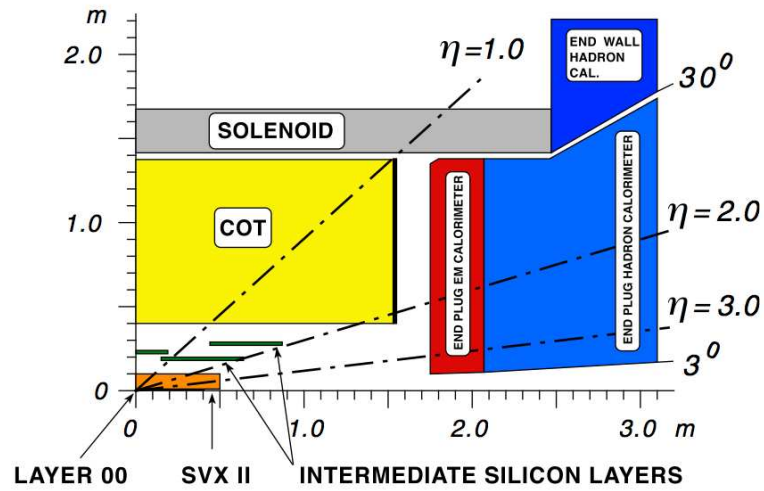


Fig. 3.3. Cross section view of the CDF II tracking and calorimetry subsystems.

3.3 The Tracking System

The tracking system is composed of an inner and outer tracker. The inner tracker relies on a silicon strip detector and the central outer tracker (COT) relies on a gaseous drift chamber.

3.3.1 Silicon Vertex Detector

The CDF II silicon detector consists of three subdetectors, each using different silicon sensor designs and layouts:

- SVX (Silicon Vertex Detector) is the core of the silicon tracking system. The innermost SVX layer is located at 2.5 cm and the outermost at 10.6 cm from the beam.
- ISL (Intermediate Silicon Layers) serves as a link between the inner silicon tracking region and the outer wire tracker. The 1.9 m long ISL consists of two layers of double-sided small angle stereo (1.2°) ladders at radii of 20 cm and 28 cm.
- L00 (Layer 00) is a single-sided layer of 48 ladders mounted at 1.5 cm from the beamline directly on the beampipe.

3.3.2 Central Outer Tracker

The Central Outer Tracker (COT) is a cylindrical open-cell drift chamber, that is located between the TOF and inner silicon tracker in the radial range from 40 cm to 138 cm. In z it extends from -155 cm to +155 cm, providing full coverage for $|\eta| < 1$ and has a maximum acceptance of $|\eta| < 2.0$.

3.4 Calorimeter

CDF calorimeters have the purpose of measuring the energy of charged and neutral particles produced in the interaction. Therefore, they also provide a measure of the energy of particles leaving the detector without interacting, by measuring the transverse energy imbalance in the detector(\cancel{E}_T). The calorimeters extend to $|\eta| < 3.6$.

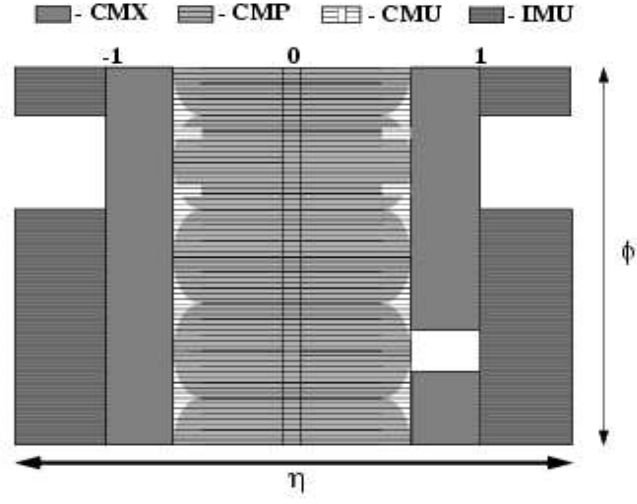


Fig. 3.4. Map of the muon coverage as a function of azimuthal angle ϕ and pseudorapidity η

3.5 Muon Detector

Muons are capable of transversing large amounts of material, before losing a significant amount of energy. In contrast to muons, the majority of particles produced in $p\bar{p}$ collisions are absorbed by the calorimeter material. Hence, the muon system is the outermost layer of our detector. To purify the muon sample, additional layers of steel absorber are placed immediately after the calorimeter and the magnet return yoke.

The CDF muon systems provide combined coverage in the rapidity interval $|\eta| < 1.5$ [Fig. 3.4].

3.6 Time of Flight Detector

The ionization energy loss, measured through dE/dx in the Central Outer Tracker, can be used for particle identification. The dE/dx measurement provides about one standard deviation separation between charged kaons and charged pions for momenta greater than 2 GeV/c .

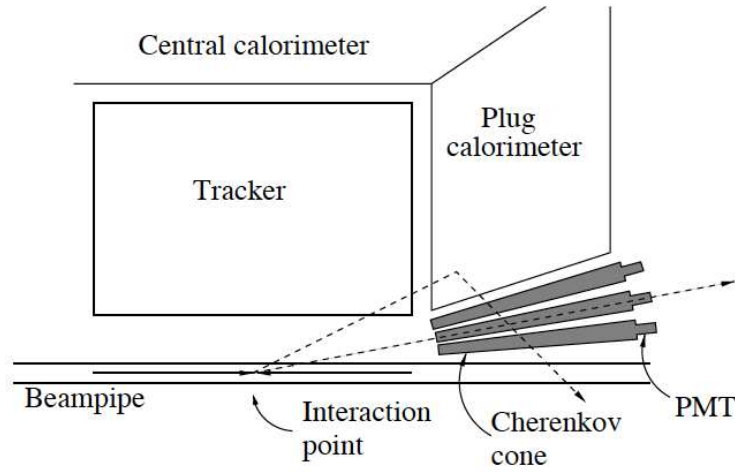


Fig. 3.5. Schematic view of the luminosity monitor

In combination with the momentum measurement p from the tracking system, the TOF detector provides particle identification by determining the particles mass. The TOF system achieves a resolution of 100 ps, which allows for at least two standard deviation separation between K^\pm and π^\pm for momenta $p < 1.6 \text{ GeV}/c$, complementing the dE/dx measurement from COT.

3.7 Luminosity Counting

The luminosity at CDF it is measured using low pressure gaseous Cherenkov counters placed at small angles relative to the beam direction. The CLC luminosity monitoring detector is composed of a well segmented array of counters shown schematically in Figure 3.6.

3.8 Trigger and Data Acquisition

The interaction rate at CDF is orders of magnitude higher than the rates that the data acquisition system can handle. Furthermore, the majority of collisions are not of interest. This leads to implementation of a system that preselects events online and decides if the corresponding detector data of an event is written to tape or discarded. This is the task of the trigger system which evaluates if a given event should be read out, reconstructed and stored. The CDF trigger system consists of three trigger levels, at which decisions based on increasingly more complex event information are made. Level 1 (L1) and Level 2 (L2) are hardware based systems while the Level 3 (L3) filters resemble the offline reconstruction code. L1 and L2 only hold a subset of event data, on which they make a decision either to pass it on for subsequent processing or to reject it.

If an event is accepted at Level 2 the entire detector is read out and processed in the Level 3 trigger which consists of a Linux PC farm, where the events are reconstructed and a final Level 3 trigger decision is made. This leads to a further reduction in the output rate by about a factor four. Events that satisfy the Level 3 trigger requirements are then transferred to the mass storage.

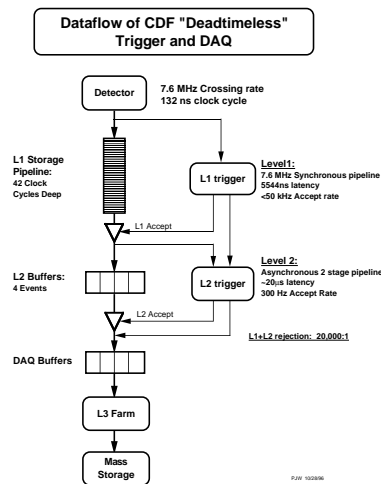


Fig. 3.6. Block diagram showing the CDF Run II trigger system

4. ANALYSIS

4.1 Event Selection and Trigger Path

4.1.1 Event Kinematics

The dominant decay mode of the SM Higgs boson with mass below 135 GeV is to two b-quarks. These quarks are detected in the calorimeters as showers of particles, or jets. The Z boson has a larger variety of decay modes. We are interested in those modes in which the Z decays to neutrinos. Since the neutrinos cannot be detected, their transverse momentum is missing from the total transverse momentum of the event, thus the main characteristic of these events is a large imbalance in the transverse energy, called Missing Transverse Energy (\cancel{E}_T). The same statement holds for the WH events when the lepton produced in the W-decay escapes detection. For similar reasons, the semi-leptonically decaying b-quarks also increase the \cancel{E}_T of an event. Whereas the azimuthal direction of the missing energy points along the jet of a semi-leptonically decaying b-quark; \cancel{E}_T induced by the neutrinos or other undetected leptons from the Z/W decays makes a larger angle to both the two b-jets. Another important characteristic of the signal is the lack of any isolated leptons.

4.1.2 Trigger Path and Data Sample

The trigger path used in this analysis is called MET35_&_TWO_JETS, which triggers on \cancel{E}_T and two jets (this trigger was changed several times during data taking period, differences are described below).

CDF has collected and processed about 1.7 fb^{-1} of data with this trigger. The amount of useful data depends on which detector system of CDF is required to be fully functional during data acquisition. For this analysis we require the silicon tracking

system and the calorimeters to be functional, since the calorimetry is needed for the jet reconstruction and electron identification, and the tracking is used for the b-tagging and isolated track recognition.

We also apply a set of quality cuts developed for \cancel{E}_T triggered events (\cancel{E}_T Clean-up) to clean up the events

4.1.3 \cancel{E}_T Clean-up

The critical part of the trigger is the \cancel{E}_T requirement. Imbalance in the total transverse energy can be caused by undetected particles, but also by some measurement effects such as beam halo muon bremsstrahlung in the detector, cosmic particle showers, detector inefficiencies, presence of hot towers and cracks in the calorimeter. These effects have been studied by the \cancel{E}_T working group of CDF. The group released a CDF note which explains how they can be minimized. Here we only quote a summary of the cuts:

- At least one central jet ($|\eta_d| < 0.9$) with $E_T > 10 \text{ GeV}$ (where η_d is the detector η).
- Event Electromagnetic Fraction (EEMF):

$$EEMF = \frac{\sum_{j=1}^{N_{jet}} E_T^j \cdot EMF_j}{\sum_{j=1}^{N_{jet}} E_T^j} > 1 \quad (4.1)$$

where EMF_j is the fraction of the jet energy deposited in the electromagnetic calorimeter. Only jets with $E_T > 10 \text{ GeV}$ are considered.

- Event Charge Fraction (ECHF):

$$ECHF = \frac{\sum_{j=1}^{N_{jet}} CHF_j}{N_{jet}} > 0.1 \quad (4.2)$$

where CHF_j is the jet charge fraction which is defined as the ratio of the sum of the p_T of the tracks matched to matching to the jet energy E_T .

- Exclude a geometrical region of the calorimeter, where jets would be mis-measured, called the 'chimney', which is a hole in the calorimeter that hosts cryogenic and instrumental connections to the inner detector.
- At least one good primary interaction vertex in the event within $|z| < 60$ cm of the nominal interaction point at the detector center.

It was found that the previous selection criteria are sufficient to eliminate the effects of the muon beam halo, therefore no further treatment is required.

4.1.4 Jet E_T and \cancel{E}_T Reconstruction

The raw jet energies and \cancel{E}_T have been used in the \cancel{E}_T quality cuts. The standard CDF jet clustering algorithm is used [4] with a jet cone of radius 0.4¹. Jet energies are corrected for calorimeter non-uniformity, non-linearity and energy loss in the un-instrumented regions of calorimeter and energy coming from different $p\bar{p}$ interactions during the same bunch crossing.

Then the event \cancel{E}_T is corrected using the new jet E_T values with the following formula:

$$\cancel{E}_x^{Corr} = \cancel{E}_x^{Raw} - \sum_i (E_x^{Corr,i} - E_x^{Raw,i}) \quad (4.3)$$

$$\cancel{E}_y^{Corr} = \cancel{E}_y^{Raw} - \sum_i (E_y^{Corr,i} - E_y^{Raw,i}) \quad (4.4)$$

The azimuth of \cancel{E}_T in the transverse plane is calculated as:

$$\varphi_{\cancel{E}_T} = \arctan \left(\frac{\cancel{E}_y^{Corr}}{\cancel{E}_x^{Corr}} \right) \quad (4.5)$$

4.1.5 B-tagging

There are different approaches to identifying jets that originate from the hadronization of b-quarks. We use SecVtx [5] algorithm used at CDF.

¹Cone algorithms form jets by associating together particles whose trajectories lie within a circle of specific radius R in $\eta \times \phi$ space, where $R = \sqrt{(\Delta\eta)^2 + (\Delta\phi)^2}$

SecVtx finds long lifetime b-hadrons which have decay lengths large enough to be detected by CDF's silicon vertex detector^{4.1}. This algorithm reconstructs the secondary vertex using tracks with large impact parameter d_0 , associated with a jet and a common primary vertex, that needs to be precisely known. The average lifetime of a b-hadron is given by $c\tau \simeq 450 \mu m$. The actual decay length $\Delta l = c\tau \cdot \beta\gamma$ is on the order of several mm, due to the Lorentz boost.

We use two categories of b-tagging algorithm [6], tight and loose. The main difference between the loose and tight tagging algorithms is that the loose tagger has more efficient track selection. The b-tagging efficiency for tight (loose) tagger is $\sim 40\%$ (50%) and mistag rate is $\sim 2\%$ (4%).

The b-tagging efficiency was measured for data and Monte Carlo and found to be higher for Monte Carlo. Hence, we apply a scale factor SF to scale the Monte Carlo to match the data. The scale factor was measured to be $SF = 0.95 \pm 0.04$ for tight tagger and 0.95 ± 0.05 for loose.

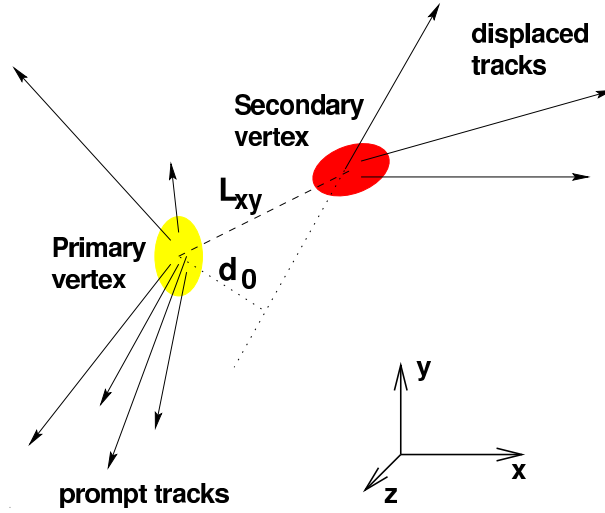


Fig. 4.1. Schematic view of the secondary vertex tagging algorithm

4.1.6 Pre-selection cuts

Events passing the quality cuts are further required to pass a set of basic selection criteria. These events will constitute the control regions and the signal region. The main motivation for the cuts is derived from the properties of the signal and the trigger path.

It was found that the systematic uncertainties originating from the choice of the trigger samples are unacceptably large at small \cancel{E}_T , thus we require every event to have \cancel{E}_T above 50 GeV. Also, the fraction of the signal events with small \cancel{E}_T is negligible with respect to the QCD multi-jet background. However, with a reliable background simulation above this threshold, we can optimize the selection cuts in a way so that QCD becomes a minor background with respect to other processes of smaller cross-sections.

Because of the change in the trigger path, an offline central jet is needed in each event. It has been shown that due to the deteriorating tagging efficiency in the non-central region of the detector and the fact that jets in the signal events tend to be central, we can extend the explicit centrality requirement to the entire $1.7^{-1}fb$ data range without measurable loss in signal efficiency.

We require the events to contain only two jets with corrected $E_T > 20$ GeV within $|\eta| < 2.4$ and discard events containing further jets with corrected energy above 20 GeV to suppress the QCD multi-jet and Top backgrounds. The efficiency of the two jet selection does not reach 100% unless the leading jet E_T is above 35 GeV and the second leading jet is above 25 GeV. In both cases, the pseudo-rapidity of the jets are below 2.0.

The last step of the pre-selections is to discard events with no positively b-tagged jets. We use two categories of b-tagging. First we look for 2 jets tagged by SecVtx loose tagger. If this fails we look for at least one jet which is tagged by SecVtx tight tagger.

4.2 Signal and Background Simulation

4.2.1 Signal Monte Carlo

The signal Monte Carlo samples are generated with Pythia [7] and reconstructed with CDF-soft version 6.1.4mc set to realistic (run-dependent) mode.

Table 4.1 lists the various mass points at which the Higgs bosons were generated, the branching fraction of the Higgs boson to b-quarks, and the corresponding $\sigma(ZH) \cdot \text{Br}(Z \rightarrow \nu\bar{\nu}, H \rightarrow b\bar{b})$ or $\sigma(WH) \cdot \text{Br}(W \rightarrow l\nu, H \rightarrow b\bar{b})$ effective cross-sections.

Higgs Mass (GeV)	$Br(H \rightarrow b\bar{b})$	$\sigma(ZH) \cdot Br(\nu\bar{\nu}, b\bar{b})$ (fb)	$\sigma(WH) \cdot Br(l\nu, b\bar{b})$ (fb)
110	0.770	19.19	53.37
115	0.732	15.78	43.50
120	0.679	12.70	34.70
125	0.610	9.92	26.89
130	0.527	7.49	20.14
135	0.436	5.43	14.46
140	0.344	3.76	9.93
150	0.176	1.48	3.72

Table 4.1

The cross-section of the ZH/WH processes at various Higgs masses, the branching fractions $Br(Z \rightarrow \nu\bar{\nu}) = 0.2$ and $Br(W \rightarrow l\nu) = 0.32$ taken into account (i.e. number of Higgs produced in the 1 fb^{-1} data)

4.2.2 Background Simulation

In the signal events the Higgs decays into two b-jets, the Z-boson into two neutrinos, and the W to leptons. The most important characteristics of these events are the large intrinsic missing transverse energy, relatively low jet multiplicity, and the lack

of (detectable) isolated leptons. There are numerous Standard Model processes that can produce this signature. In this section, we list all the backgrounds considered in the analysis (see Table 4.2).

Process	Events	Cross-section(pb)	Luminosity (fb^{-1})
QCD mutli-jet	1932M	4.4×10^5	3.11
$t\bar{t}$	988K	7.3	135.4
single top (s-channel)	254K	0.88	289
single top (t-channel)	259K	1.98	131
W^\pm to $e^\pm \nu$	30.3M	1959	11.0
W^\pm to $\mu^\pm \nu$	56.3M	1982	20.3
W^\pm to $\tau^\pm \nu$	26.3M	1971	9.54
Z to $e^- e^+$	10.4M	355	21.0
Z to $\mu^- \mu^+$	10.4M	355	21.0
Z to $\tau^- \tau^+$	5.1M	355	10.3
Z to $\nu \bar{\nu}$	62.5M	1102	40.5
WW to all	519K	12.0	43.3
WZ to all	520K	3.64	143
ZZ to all	521K	3.32	157

Table 4.2
Monte Carlo background samples

QCD multi-jet background

QCD jet production has a large cross-section ($\sim \mu b$), which is about 9 orders of magnitude greater than the signal. Although, these processes generally do not have intrinsic \cancel{E}_T , mismeasured jets do cause imbalance in the total transverse energy by which the QCD events can pass the basic selection cuts if one of the jets is mis-tagged.

Furthermore, QCD b-quark pair production yields taggable jets and if one b undergoes a semi-leptonic decay large \cancel{E}_T . In both cases, the missing transverse energy tends to be aligned parallel or anti-parallel to the first or second most energetic jet. This topology provide us the most effective device against the QCD background.

Due to the large cross-section, it is practically impossible to generate enough statistics to simulate all QCD processes. In this analysis, we simulate processes which yield real taggable objects, that is, when a b- or a c-quark pair is created. The rest of the QCD processes, after requiring a positive tag in the event during the basic selections, are considered to be light flavor jets (mistags) and are treated separately.

Top

Two classes of top-production are considered in this analysis. The pair-production and the single top production in the t- and s-channels. They all yield a measurable contribution to the background in the signal region, but the pair-production is the most significant. The single top background becomes more relevant after requiring only two hard jets in the event. Due to its large mass and the semi-leptonic decay of the top, these events are energetic, bear large \cancel{E}_T and high jet multiplicity.

Di-boson and W/Z backgrounds

The electroweak backgrounds were all generated with Pythia. All the W and Z samples were filtered for a b- or c-quark at generator level with the exeption of $W \rightarrow \tau\nu$ and $Z \rightarrow \tau\bar{\tau}$. In the diboson simulations, the bosons' decays are all-inclusive.

Mistagged Light Flavor Background

The falsly tagged light flavor, or otherwise called mistag, multi-jet processes constitute one of the largest SM background in the single tag sample. However, its

significance is greatly reduced after requiring a second tag in the event. We estimate this component from the data by applying the Mistag matrix to it after the events pass the pre-selection cuts.

The Mistag matrix is a multi dimensional matrix, the elements of which predict the probability that a generic jet with a certain E_T , η and N_{trk}^{good} in an event with a given $\sum E_T$, vertex number and Z-position of the primary vertex is b-tagged. Summing this probability for each taggable jet, one computes the weight of the event that corresponds to the rate at which such event contains a mistagged jet; by reweighting the events when filling histograms one can compute the predicted distribution of any observables.

4.3 Control and Signal Region Definitions

Selected events are divided into three regions: two control regions and the signal region in which the normalizations and the shapes of various simulated background processes can be compared to the data. Data - Monte Carlo comparisons have been performed in the signal region after determining the final cuts based on the simulated events to keep the analysis ‘blind’.

4.3.1 Definition of Control Regions

The most important property of the QCD multi-jet events is that the \cancel{E}_T tends to be parallel or anti-parallel to the first or to the second leading jet. In the signal, this angle peaks around 120° ; therefore, cutting on this variable yields an excellent separation between the signal and the QCD background. Also, QCD multi-jet processes do not produce isolated leptons. By vetoing them, we can separate this process from most of the other Standard Model backgrounds. The rest of the SM backgrounds do produce isolated leptons, with the exception of Z decaying into neutrinos. These backgrounds are cross-checked in a second control region.

The definition of the control regions and the signal region is as follows (see Fig.??):

- Control Region 1 (QCD dominated)
 - All leptons are vetoed using the loose lepton identifications described later in the next section
 - Azimuthal angular separation $\varphi(2^{nd}jet, \cancel{E}_T) \leq 0.4$
- Control Region 2
 - Minimum 1 loose lepton is required
 - Azimuthal angular separation $\varphi(2^{nd}jet, \cancel{E}_T) > 0.4$
- Signal Region
 - Leptons are vetoed
 - Azimuthal angular separations $\varphi(2^{nd}jet, \cancel{E}_T) > 0.4$ and $\varphi(1^{st}jet, \cancel{E}_T) > 0.4$

Process	1 Tight tag	2 Loose Tags
QCD h.f.	$24337.1 \pm 111.4 \pm 5445.4$	$3768.5 \pm 45.8 \pm 688.2$
Top	$7.1 \pm 0.4 \pm 0.8$	$2.3 \pm 0.2 \pm 0.4$
Di-boson	$1.1 \pm 0.2 \pm 0.2$	$0.1 \pm 0.1 \pm 0.1$
W + h.f.	$26.2 \pm 2.7 \pm 11.1$	$1.1 \pm 0.5 \pm 0.4$
Z + h.f.	$8.7 \pm 1.2 \pm 3.6$	$0.9 \pm 0.4 \pm 0.4$
Mistag	$6181.0 \pm 63.6 \pm 498.5$	$415.2 \pm 10.0 \pm 71.1$
Total bckg	30561.2 ± 5469.7	4188.1 ± 693.4
Observed	29431	4190

Table 4.3
Number of expected background events in the QCD control region

Process	1 Tight tag	2 Loose Tags
QCD h.f.	$50.7 \pm 5.1 \pm 12.6$	$7.0 \pm 2.0 \pm 1.9$
Top	$134.8 \pm 1.6 \pm 16.4$	$55.9 \pm 1.0 \pm 9.0$
Di-boson	$14.7 \pm 0.8 \pm 2.5$	$1.9 \pm 0.2 \pm 0.4$
W + h.f.	$80.5 \pm 4.1 \pm 34.9$	$8.2 \pm 1.3 \pm 3.6$
Z + h.f.	$17.5 \pm 1.8 \pm 7.9$	$1.3 \pm 0.5 \pm 0.7$
Mistag	$86.5 \pm 4.3 \pm 6.3$	$3.7 \pm 1.2 \pm 0.8$
Total bckg	384.7 ± 42.6	77.9 ± 10.3
Observed	373	79

Table 4.4
Number of expected background events in the EWK control region

Lepton Identification

The goal of the lepton identification in this analysis is to obtain the best possible efficiency in recognizing a lepton. Since we do not need a high purity lepton sample, but indeed the opposite, we use a set of loose identification cuts to reject events with isolated leptons.

Events with identified leptons comprise of events with real isolated leptons, those with real non-isolated leptons incorrectly classified as isolated, and events with tracks that fake isolated leptons. W/Z + jet processes are an example for the first case, and QCD h.f. production for the second and third.

4.3.2 Control Region 1

This region indicates how well the simulation describes the heavy flavor QCD multi-jet processes and corroborates the normalization of the Monte Carlo to the data.

Control Region 1 (CR-1) has a slightly different composition of heavy flavor production modes than the Signal Region due to the cut on $\varphi(2^{nd}jet, \cancel{E}_T)$. When the b-quarks are back-to-back (e.g. in b-quark production in the hard scattering), the \cancel{E}_T originates from mismeasuring one or more jets. The difference between the E_T of the leading and second leading jets is large, because in the back-to-back topology the mismeasurements of the jets balance each other to some extent (mismeasurement generally means underestimation). By requiring the second jet to pass a minimum threshold (in our case 25 GeV) and the event to have large \cancel{E}_T simultaneously, we bias the leading jets high. Also, the prediction of this region by our simulation is very susceptible to the jet energy scale. (JES is one of the biggest uncertainties in \cancel{E}_T based analyses.)

In contrast, the Signal Region contains more events where the b-quarks are produced by gluon-splitting. In such cases, the b-jets are not back-to-back and their mismeasurements do not cancel each other; therefore, the leading jet in the Signal Region tends to be less energetic. The composition of these two cases determines the shape of the jet E_T distributions in both Control and Singal Regions. The leading jet distribution in the Signal Region is a composition of an exponentially decreasing function and one with a peak at higher E_T . The uncertainty due to the $\varphi(2^{nd}jet, \cancel{E}_T)$ cut introduces an uncertainty in this shape.

Table 4.3 list the number of events that pass the pre-selection and control region definition cuts in the Exclusive Single and Double tag samples. Figures 4 and 5, show comparions of various observables between the data and the simulation.

4.3.3 Control Region 2

This control region is a mix of various SM processes. The double tag events are dominated by top production which provides an individual check for the top background simulation. We observe a good agreement with the data. The expected

number of events are shown in Table 4.4 and Figures 6 and 7, show comparisons of various observables between the data and the simulation.

4.3.4 Signal Region

We used the 115 GeV Higgs samples to demonstrate the acceptance of the cuts in the signal region. The result is shown in Table ??.

Process	Single Tag	Double Tags
QCD h.f.	$157.4 \pm 9.0 \pm 49.1$	$10.6 \pm 2.4 \pm 3.9$
Top	$48.2 \pm 1.0 \pm 4.1$	$14.0 \pm 0.5 \pm 2.1$
Di-boson	$11.5 \pm 0.6 \pm 2.4$	$1.9 \pm 0.2 \pm 0.4$
W + h.f.	$59.9 \pm 4.1 \pm 26.6$	$4.6 \pm 1.1 \pm 2.0$
Z + h.f.	$28.3 \pm 1.9 \pm 12.5$	$4.1 \pm 0.7 \pm 1.9$
Mistag	$98.2 \pm 7.3 \pm 12.8$	$4.7 \pm 1.0 \pm 1.1$
Total bckg	403.5 ± 60.1	39.9 ± 6.1
Observed	443	51
$(VH \ m_H = 115 \text{ GeV}/c^2)$	(1.9)	(1.2)

Table 4.5
Number of expected background and signal events in the signal region after applying the final cuts.

Final Selection

Currently, a set of orthogonal cuts are used in the final optimization. In the future, a more efficient optimization is going to be used with which it might be possible to lower the \cancel{E}_T threshold thus increasing the signal acceptance. Developing such an optimization is a challenge, since the \cancel{E}_T cut represents by far the best separation power after requiring tags, cutting on the angles between jets and \cancel{E}_T , and selecting

a mass-window. An effective signal optimization also requires large statistics in the background simulation which is not always available using the current method. We are now working on a new method that could be used to estimate the QCD multi-jet background directly from the data. This improvement would solve the most significant problem at the present, the QCD Monte Carlo production, and would provide an opportunity to focus on further improvements. The final result, nevertheless, is mostly limited by the data statistics in the double tags, therefore these improvements will gain significance when more data is processed.

The final selection is as follows:

- Azimuthal separation between leading jet and \cancel{E}_T : $(1^{st}jet, \cancel{E}_T) > 0.8$ rad
- $\frac{\cancel{E}_T}{H_T} > 0.45$
- E_T of leading jet: $1^{st}jet E_T > 60$ GeV
- $\cancel{E}_T > 70$ GeV

The number of background events after the final selection is shown in Table 4.6. We expect a total of 1.8 Higgs events (mass 115 GeV) in the single and 1.1 in the double loose tagged data given by the sum of ZH and WH events from the last two lines of Table ??.

4.4 Systematic Uncertainties and Limit Calculation

The systematic uncertainties are classified as correlated and uncorrelated errors considering the relations between the signal and the background processes. The correlated errors are taken into account separately for each processes in the limit calculation. The uncorrelated systematic uncertainties are: statistical error in negative tag estimate, negative-positive tag rate asymmetry factor, QCD multi-jet Monte Carlo normalization (14% in single tagged, 6.3% in double tagged sample), MC statistical fluctuations. The correlated systematics are: luminosity (6.0%), b-tagging

Process	Single Tag	Double Tag
QCD multi-jet	$157.4 \pm 8.96 \pm 44.03$	$10.56 \pm 2.43 \pm 3.88$
TOP	$48.21 \pm 0.97 \pm 6.85$	$13.98 \pm 0.5 \pm 2.13$
Di-boson	$11.53 \pm 0.61 \pm 2.52$	$1.93 \pm 0.18 \pm 0.41$
W + h.f.	$59.91 \pm 4.08 \pm 26.95$	$4.63 \pm 1.11 \pm 2.04$
Z + h.f.	$28.31 \pm 1.9 \pm 12.69$	$4.09 \pm 0.7 \pm 1.89$
Mistag	$98.18 \pm 7.27 \pm 31.73$	$4.71 \pm 0.81 \pm 1.0$
Total Expected BCK	403.53 ± 60.08	39.91 ± 6.09
Observed	443	51

Table 4.6
Number of expected background and signal events in the signal region after applying the final cuts.

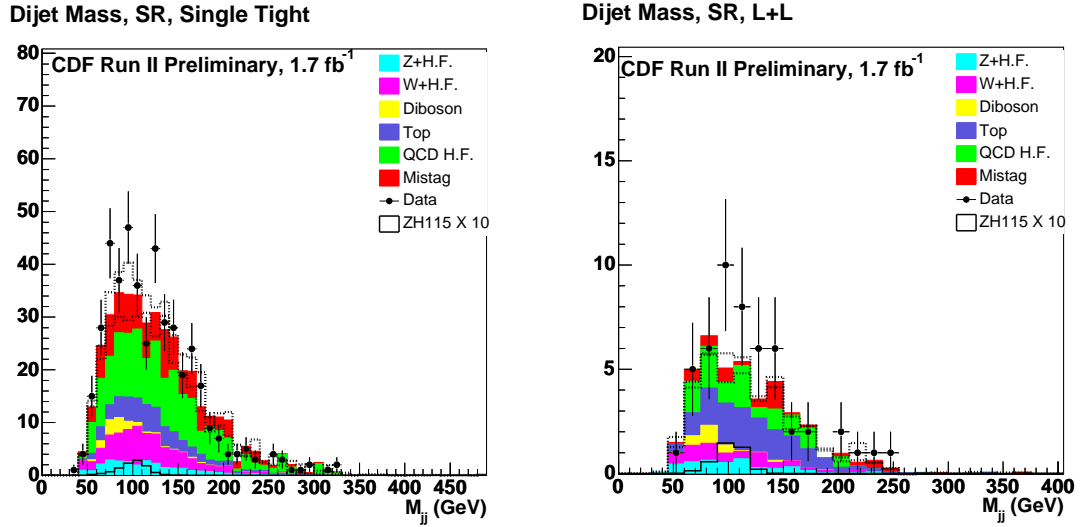


Fig. 4.2. Dijet invariant mass in the Signal Region, single- and double-tagged events

Higgs mass (GeV)	VH limit, 1 Tight Tag		VH limit, 2 Loose Tags		VH limit, Combined	
	Predicted	Observed	Predicted	Observed	Predicted	Observed
110	$19.7^{+9.7}_{-6.0}$	36.6	$10.4^{+4.4}_{-2.9}$	18.7	$9.3^{+4.4}_{-2.9}$	18.5
115	$22.7^{+9.5}_{-7.2}$	37.2	$11.1^{+4.4}_{-3.3}$	20.8	$9.7^{+5.0}_{-2.8}$	19.7
120	$27.5^{+11.4}_{-7.7}$	40.8	$13.0^{+6.5}_{-3.9}$	25.2	$11.5^{+5.5}_{-3.7}$	22.6
125	$31.2^{+14.8}_{-9.3}$	46.6	$15.9^{+6.6}_{-4.8}$	30.1	$13.4^{+6.1}_{-4.1}$	26.6
130	$40.6^{+16.7}_{-12.6}$	58.7	$19.5^{+10.6}_{-5.5}$	39.3	$16.6^{+7.3}_{-5.3}$	33.4
135	$52.0^{+22.4}_{-16.7}$	74.6	$24.7^{+10.7}_{-7.5}$	48.3	$21.0^{+9.7}_{-6.3}$	43.0
140	$71.6^{+31.5}_{-23.7}$	110.0	$35.3^{+17.5}_{-10.9}$	64.3	$31.5^{+16.4}_{-7.2}$	61.5
150	$172.3^{+71.7}_{-61.4}$	238.6	$77.1^{+37.1}_{-22.4}$	133.6	$72.1^{+30.9}_{-23.4}$	127.0

Table 4.7

The predicted and observed cross-section limits of the ZH and WH processes combined when $H \rightarrow b\bar{b}$ divided by the SM cross-section where Z decays to neutrinos and W decays leptonically

efficiency scale factor between data and Monte Carlo (4.3% for single and 10.2% for double tags), trigger efficiency (3%), lepton veto efficiency (2%), PDF uncertainty (2%) and Jet Energy Scale. ISR/FSR² systematic uncertainties (between 1% and 5%) are applied on the signal.

4.4.1 Expected and Observed Limits

Considering the systematic uncertainties listed above, we computed the expected and observed limits for the Higgs cross-section when the Higgs is produced with a Z/W boson and decays to two b-quarks where Z decays to neutrinos and W to leptons. We use Bayesian method for deriving the limits [8]. Table 4.7 shows the final result. All the cross-sections are ratios with respect to the Standard Model cross-section.

²ISR: Initial State Radiation, FSR: Final State Radiation

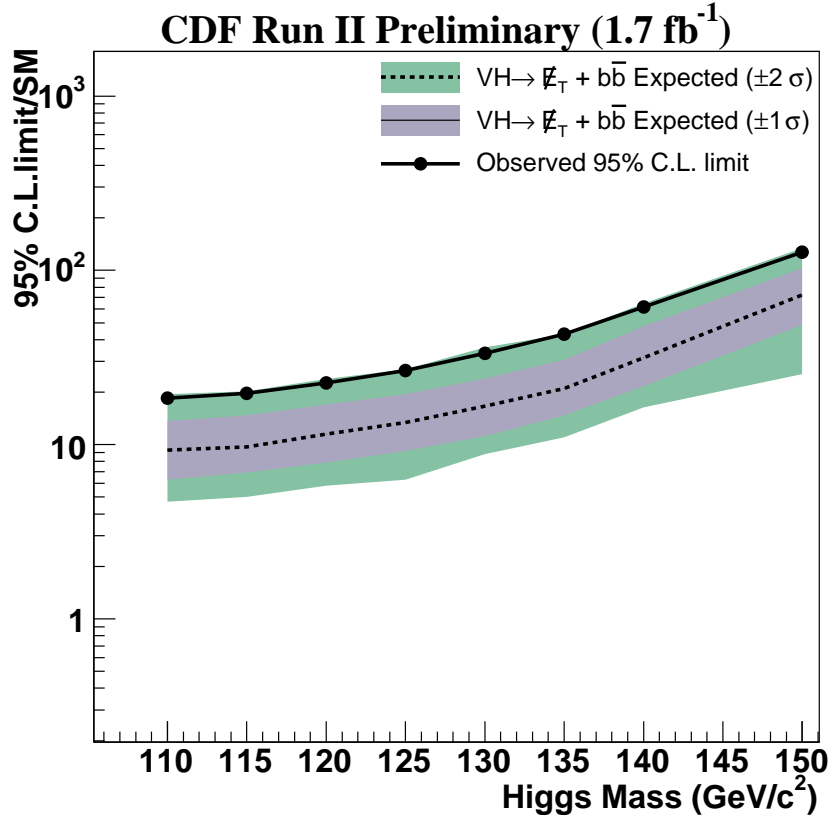
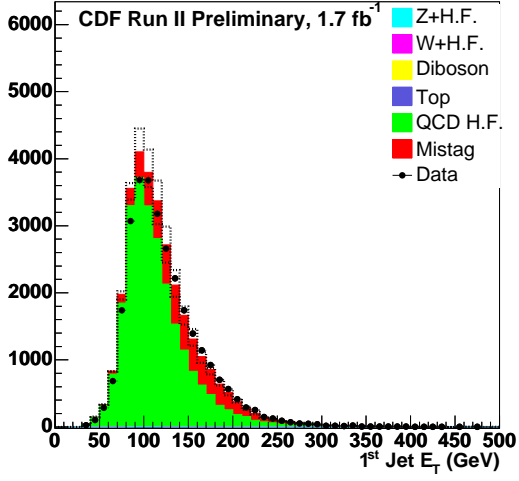


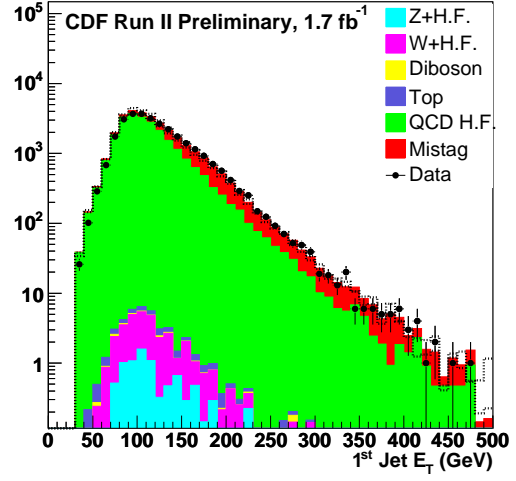
Fig. 4.3. The Cross-Section upper limits

APPENDIX

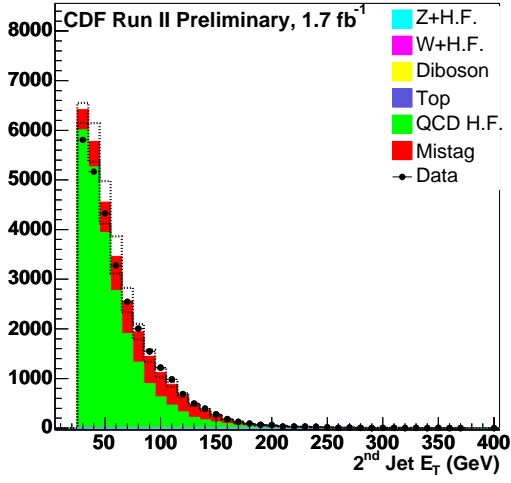
Leading Jet E_T , CR1, Single Tight tag



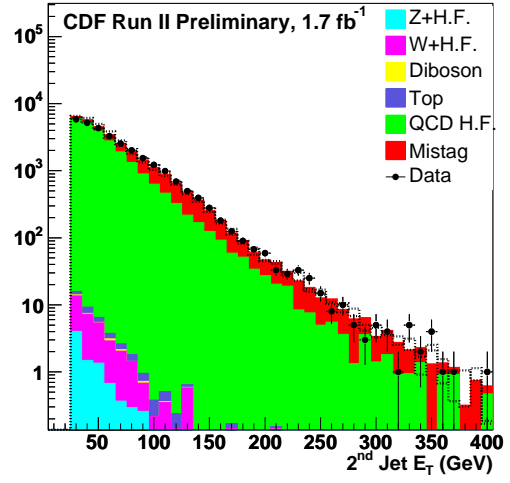
Leading Jet E_T , CR1, Single Tight tag



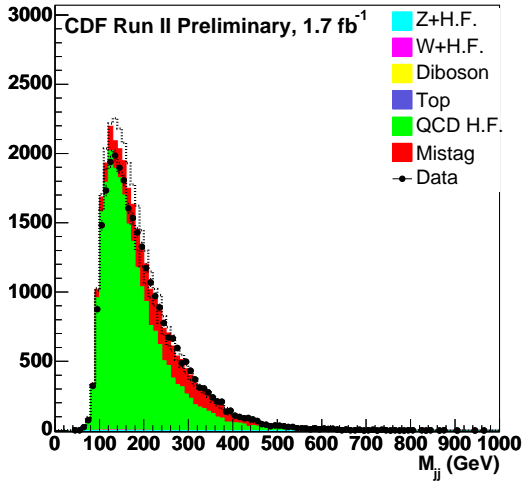
Second Leading Jet E_T , CR1, Single Tight tag



Second Leading Jet E_T , CR1, Single Tight tag



Dijet Mass, CR1, Single Tight



Dijet Mass, CR1, Single Tight

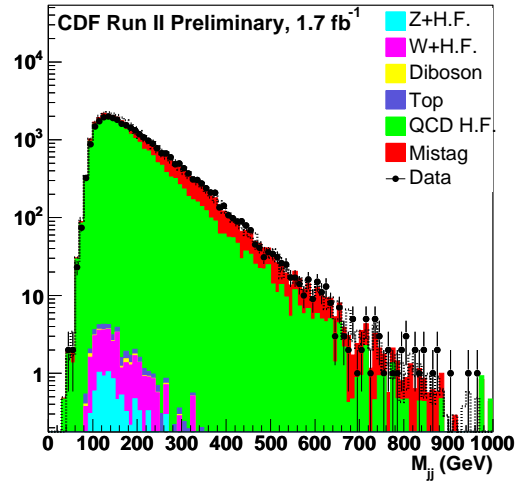
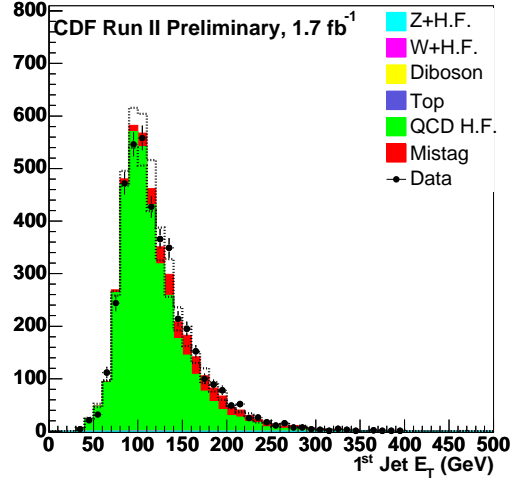
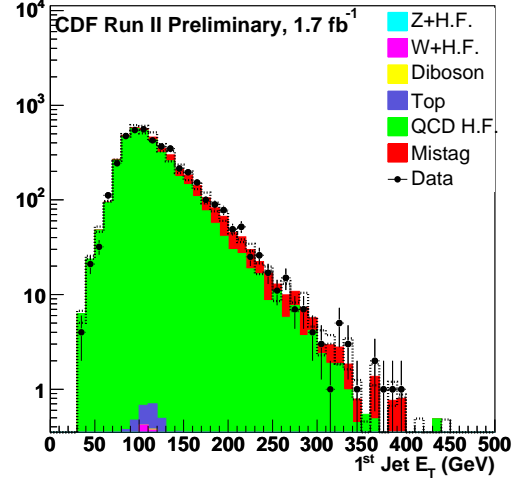


Fig. 4. Control Region 1, Exclusive Single Tag plots from the top: 1st jet E_T , 2nd jet E_T , dijet mass

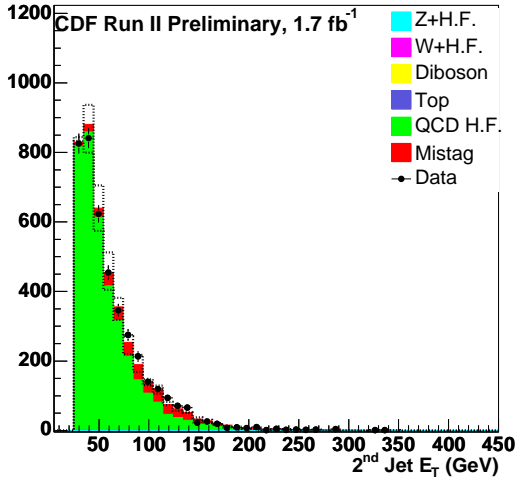
Leading Jet E_T , CR1, L+L tag



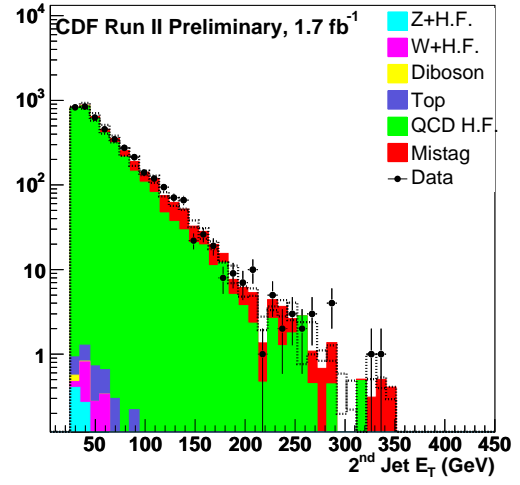
Leading Jet E_T , CR1, L+L tag



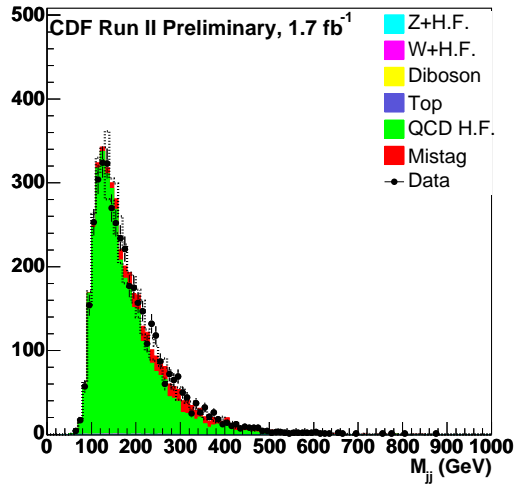
Second Leading Jet E_T , CR1, L+L tag



Second Leading Jet E_T , CR1, L+L tag



Dijet Mass, CR1, L+L



Dijet Mass, CR1, L+L

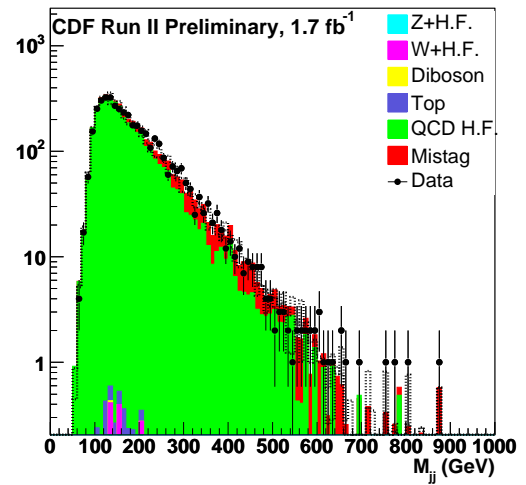
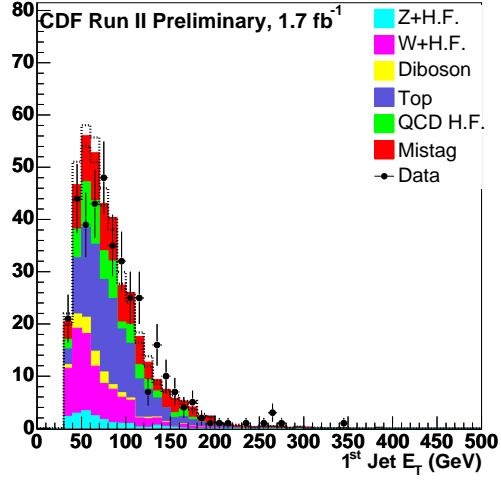
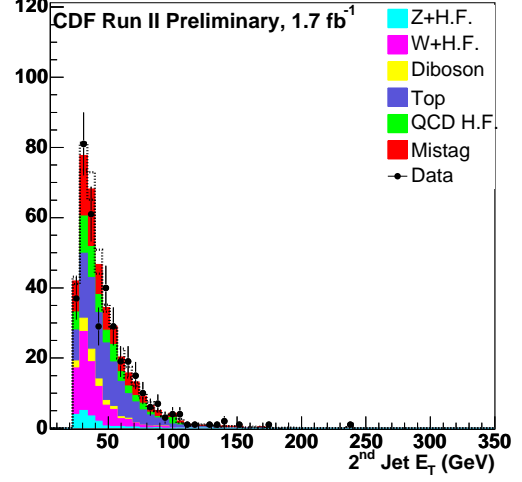


Fig. 5. Control Region 1, Double Loose Tag plots from the top: 1^{st} jet E_T , 2^{nd} jet E_T , dijet mass

Leading Jet E_T , CR2, Single Tight tag



Second Leading Jet E_T , CR2, Single Tight tag



Dijet Mass, CR2, Single Tight

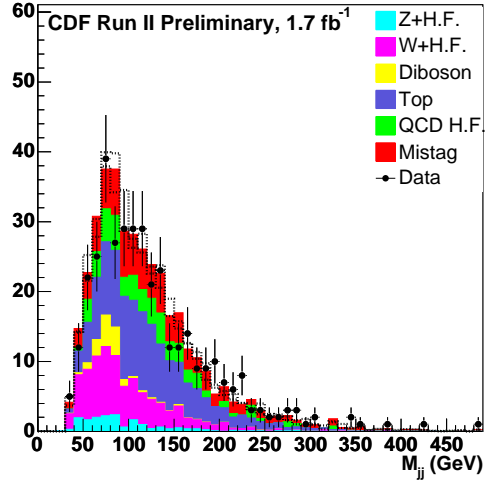
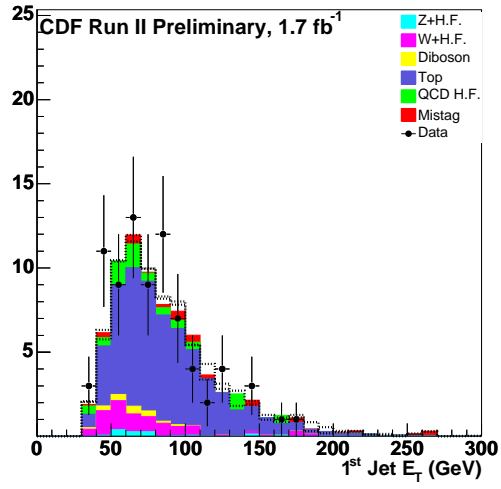
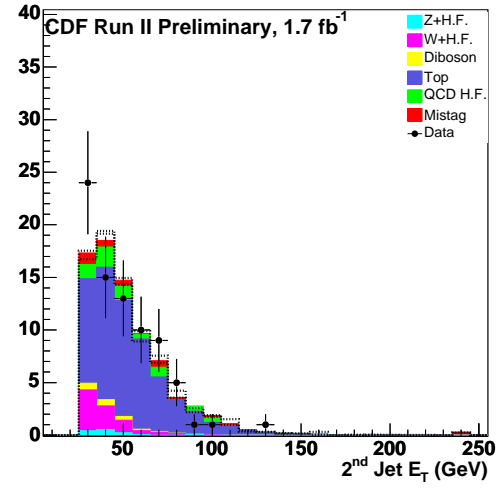


Fig. 6. Control Region 2, Exclusive Single Tag plots after tight lepton selection from the top: 1^{st} jet E_T , 2^{nd} jet E_T , dijet mass

Leading Jet E_T , CR2, L+L tag



Second Leading Jet E_T , CR2, L+L tag



Dijet Mass, CR2, L+L

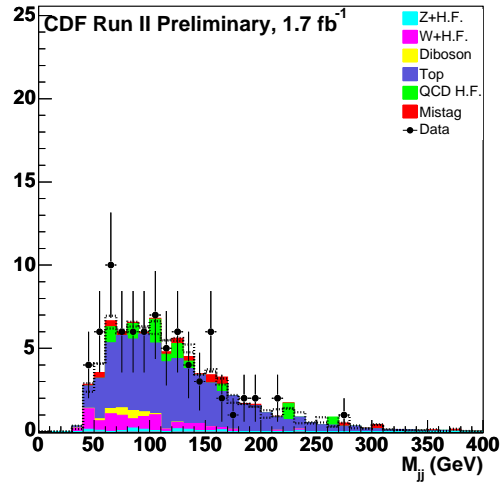


Fig. 7. Control Region 2, Double Tag plots after tight lepton selection from the top: 1st jet E_T , 2nd jet E_T , dijet mass

A. SUMMARY

We have performed a direct search for the Standard Model Higgs boson decaying into b-jet pairs in 1.7 fb^{-1} data accumulated in Run II of the CDF detector. We do not observe any significant excess over the background predicted by the Standard Model, thus we set a 95 % C.L. upper limit for the Higgs boson at various masses. The observed cross-section limits agree with the expected ones within 2σ .

LIST OF REFERENCES

LIST OF REFERENCES

- [1] J. Gunion et al., *The Higgs Hunter's Guide*. Reading Massachusetts: Addison-Wesley, second ed., 1990.
- [2] A.I.Veinstein *Sov. Phys. Usp.*, vol. 23, p. 429, 1980.
- [3] R. Blair *et al.*, (CDF Collaboration), *The CDF-II Detector Technical Design Report*, Fermilab- Pub-96/390-E (1996).
- [4] F.Abe et al. *Phys. Rev. D*, vol. 45, p. 1448, 1992.
- [5] <http://cdfcodebrowser.fnal.gov/CdfCode/source/VertexAlg/doc/ctvmft.txt>.
- [6] D. Acosta et al. *Phys. Rev. D.* 71, vol. 71, p. 052003, 2005.
- [7] Torbjorn Sjostrand and Leif Lonnblad and Stephen Mrenna, "Pythia 6.2 - physics and manual."
- [8] T. Junk, "Exclusion and Discovery with Small Signals, Large Backgrounds, and Large Systematic Uncertainties," *CDF/DOC/STATISTICS/PUBLIC/8128*.